ELSEVIER

Ocean Modelling 5 (2003) 37–63

Ocean Modelling

www.elsevier.com/locate/omodol

A diagnostic stabilized finite-element ocean circulation model

Dmitri Nechaev [a,*], Jens Schröter [b], Max Yaremchuk [c]

[a] Department of Marine Science, University of Southern Mississippi, Stennis Space Center,
1020 Balch Boulevard, MS 39529, USA
[b] Alfred-Wegener Institute, Postfach 120161, 27515 Bremerhaven, Germany
[c] International Pacific Research Center, Honolulu, 96822 HI, USA

Received 24 January 2001; received in revised form 22 March 2002; accepted 27 March 2002

Abstract

A stabilized finite-element (FE) algorithm for the solution of oceanic large scale circulation equations and optimization of the solutions is presented. Pseudo-residual-free bubble function (RFBF) stabilization technique is utilized to enforce robustness of the numerics and override limitations imposed by the Babuška–Brezzi condition on the choice of functional spaces. The numerical scheme is formulated on an unstructured tetrahedral 3d grid in velocity–pressure variables defined as piecewise linear continuous functions. The model is equipped with a standard variational data assimilation scheme, capable to perform optimization of the solutions with respect to open lateral boundary conditions and external forcing imposed at the ocean surface. We demonstrate the model performance in applications to idealized and realistic basin-scale flows. Using the adjoint method, the code is tested against a synthetic climatological data set for the South Atlantic ocean which includes hydrology, fluxes at the ocean surface and satellite altimetry. The optimized solution proves to be consistent with all these data sets, fitting them within the error bars.

The presented diagnostic tool retains the advantages of existing FE ocean circulation models and in addition (1) improves resolution of the bottom boundary layer due to employment of the 3d tetrahedral elements; (2) enforces numerical robustness through utilization of the RFBF stabilization, and (3) provides an opportunity to optimize the solutions by means of 3d variational data assimilation. Numerical efficiency of the code makes this a desirable tool for dynamically constrained analyses of large datasets.

Keywords: Finite elements; Pseudo-residual-free bubbles; Stabilization methods; Ocean modeling

---

[*] Corresponding author. Tel.: +1-228-688-3177; fax: +1-228-688-1121.

E-mail addresses: dnechaev@ssc.usm.edu (D. Nechaev), jschroeter@awi-bremerhaven.de (J. Schröter), maxy@soest.hawaii.edu (M. Yaremchuk).

PII: S1463-5003(02)00013-6

1. Introduction

Traditionally, ocean general circulation models (OGCMs) rely on the well-established finite-difference (FD) technique to discretize the equations of motion. Highly parallelized modern OGCMs which run globally on 1/4–1/6°grids still have insufficient resolution since the dynamically important scales are not resolved everywhere. Further grid refinement requires tremendous computer power which is excessive in the main because the dynamically important "small scale regions" occupy $<1\%$ of the ocean surface.

Finite-element (FE) methods, although being out of the main stream in OGCM development (Griffies et al., 2000), offer a number potential advantages compared to the FD approach. They provide flexibility of local resolution enhancement where needed, a better representation of the bottom topography, smoother coastline representation, and convenience of the numerics for parallelization and data assimilation purposes.

In engineering literature there exists a large number of 3d FE models which demonstrate perfect performance in solving the Navier–Stokes equations. FE applications to the problems of large scale ocean dynamics are much more rare (e.g. Iskandarani et al., 1995; Myers and Weaver, 1995). One may argue that problems in ocean dynamics are more complex than those in engineering: effects of the Earth's rotation introduce an additional hierarchy of scales and dynamical balances, which is complicated by the presence of the very wide spatial spectrum of the topographic scales. Griffies et al. (2000) mention two major problems with FE which may have hindered the development of FE OGCMs. The first problem is associated with the well-known difficulties in representing the geostrophic balance in combination with the divergent wave motions. The second is that inhomogeneities in grid spacing provoke unphysical wave scattering. Other effects of grid and much more complex numerics can be considered as additional factors which made FE methods less competitive compared to FD approach.

In recent years, however, there has been a significant progress in FE modeling which seems to dispel the notion that FE OGCMs are impractical for large scale ocean modeling. Le Roux et al. (1998) found a low-order element pair satisfying the Babuška–Brezzi (LBB) compatibility condition (Babuška, 1971), and having perfect properties in representing the geostrophic balance. Later this FE formulation was combined with a semi-Lagrangian scheme to produce an efficient shallow water ocean model (Le Roux et al., 2000). More importantly, a few years ago the residual-free bubble function (RFBF) stabilization methods have been developed (Pierre, 1995; Franca and Russo, 1996a; Brezzi et al., 1997). The technique can be viewed as a generalization of the numerous regularization schemes which have been widely used in literature to circumvent LBB compatibility condition. RFBF stabilization also provides a general approach to the control over the FE approximation errors and gives a promising recipe to solving the problem of unphysical wave scattering on irregular grids.

In the present study we utilize these latest developments to construct a diagnostic model of ocean circulation with the 3d tetrahedral grid. The latter feature can be also considered as a step forward in FE ocean modeling since, to our knowledge, existing models are either 2d, (Lynch and Gray, 1979; Lyard, 1997) or utilize prismatic elements (Greenberg et al., 1998) whose geometric flexibility is somewhat lower. Employment of the 3d unstructured tetrahedral grid reduces the pressure gradient errors normally seen in terrain following grids, and makes the model more flexible in the description of the bottom boundary layers and fine topographic features such as narrow straits, underwater ridges and continental slopes, which control the exchange of properties between deep water basins and may define oceanic "climate" on global scales. Other important features of the presented model include explicit FE treatment of thermodynamics and the 3d variational data assimilation scheme which allows a user to optimize the model's parameters with respect to available data.

Most of the components of the proposed model have been in use in the FE community for some time, but have not been applied together in large scale oceanic simulation. For instance, the 2d FE tidal model of Le Provost and Poncet (1978) was equipped with variational data assimilation schemes in (Lyard and Genco, 1994) and (Sentchev and Yaremchuk, 1999) while Lynch et al. (1996) combined advection of heat and salt with shallow water dynamics discretized on prismatic triangular elements.

The aim of the present study is to combine the RFBF stabilization technique and the weak Galerkin FE discretization on unstructured 3d tetrahedral mesh, and to demonstrate the feasibility of this approach for ocean modeling. The paper is organized as follows. In the next section we specify the model equations in the differential form and a weak formulation of the problem. This includes description of the RFBF stabilized numerical scheme for momentum equations and employment of the stream-line diffusion stabilization algorithm in treating of the tracer conservation constraints. In Section 3 we demonstrate application of the RFBF method to solution of the 1d Ekman problem and 2d shallow water equations in idealized basin. Section 4 contains the results of 3d simulation of the large scale circulation in the South Atlantic which is then optimized using the variational data assimilation algorithm. Conclusions are drawn in Section 5. A brief description of the RFBF stabilization technique and other technical details can be found in Appendices A and B.

2. Model description

2.1. Governing equations

The governing equations of the model describe thermo-hydrodynamics of a thin stratified layer of sea water on spherical rotating Earth under hydrostatic, Boussinesq and traditional approximation for the Coriolis terms. To avoid simultaneous treatment of non-linear dynamics and thermodynamics we split the system of equations into two subproblems and solve them separately.

The dynamical part of the model solves the steady state momentum balance equation under the integral continuity constraint,

$$f(\mathbf{k}\times\mathbf{u}) + g\nabla\zeta - \nabla\cdot A_l\nabla\mathbf{u} - \partial_z A_v\partial_z\mathbf{u} = -\frac{1}{\rho_0}\nabla p_\rho + \mathbf{F}_u, \tag{1}$$

$$\int_{z=-H}^{z=0} \nabla\cdot\mathbf{u}\,\mathrm{d}z = F_\zeta, \tag{2}$$

$$\partial_z p_\rho = -g\rho, \tag{3}$$

where $(\mathbf{u}) \equiv (u, v)$ is the horizontal velocity vector, ρ_0, ρ are the mean sea water density and the deviations from that mean respectively, ζ is the sea surface elevation, p_ρ is the baroclinic pressure anomaly, $f = f(\theta)$ is the Coriolis parameter, A_l, A_v are the lateral and vertical momentum diffusion coefficients, $\mathbf{k}$ is the vertical unit vector, and g is the gravitational acceleration. $\mathbf{F}_u$, F_ζ stand for the advection of momentum, the steady state kinematic constraint at the free ocean surface ($F_\zeta = -\mathbf{u}\nabla\zeta$) and could be taken into account iteratively.

The dynamical part of the model considers the density variation ρ to be known. Eqs. (1)–(3) are solved in a multiply connected region Ω with four physically different types of boundaries $\partial\Omega = \bigcup_{i=1}^{4} \Gamma_i$, where $\Gamma_1 : \{z = 0\}$ stands for the ocean surface, $\Gamma_2 : \{z = -H(\lambda, \theta)\}$ is the bottom of the ocean, Γ_3 denotes the lateral vertical open boundaries and the fourth type of boundaries represents the vertical rigid walls of the domain Γ_4. The boundaries Γ_4 are introduced to avoid excessive refinement of the grid in coastal areas and in the regions of large topographic gradients. The set of boundary conditions used with the dynamical model includes the condition of the momentum flux continuity on the ocean surface, Dirichlet conditions for the normal velocity component combined with free-slip conditions for the tangent velocity on the open boundaries, and no-slip boundary conditions on the rigid boundaries

$$A_v \partial_z \mathbf{u} = \boldsymbol{\tau}, \qquad p_\rho = 0 \quad \text{on } \Gamma_1, \tag{4}$$

$$\mathbf{u} = 0 \quad \text{on } \Gamma_2 \cup \Gamma_4, \tag{5}$$

$$\mathbf{u} \cdot \mathbf{n} = u_n, \qquad (\mathbf{n} \cdot \nabla)(\mathbf{u} \cdot (\mathbf{k} \times \mathbf{n})) = 0 \quad \text{on } \Gamma_3, \tag{6}$$

where $\boldsymbol{\tau}$ is the vector of tangent wind stresses, u_n is a given distribution of the normal velocity and $\mathbf{n}$ is the horizontal unit vector normal to the open boundaries.

In the second subproblem of the model we diagnose vertical velocity w from the continuity equation, solve the steady state advection–diffusion equations for tracers, and compute density via the equation of state:

$$\partial_z w = -\nabla \cdot \mathbf{u}, \tag{7}$$

$$\nabla \cdot (\mathbf{u}C^m) + \partial_z(wC^m) - \nabla \cdot K_l^m \nabla C^m - \partial_z K_v^m \partial_z C^m = 0, \tag{8}$$

$$\rho - \varrho(T, S, p) = 0. \tag{9}$$

Here $C^1 \equiv T$ is the potential temperature, $C^2 \equiv S$ is the salinity of sea water, while $C^3, \ldots, C^m$ are the passive tracer concentrations, K_l^m, K_v^m are the lateral and vertical diffusion coefficients for the mth tracer and ϱ denotes the non-linear operator of the sea water equation of state proposed by Ishizaki (1994). In the presented version of the model w is used solely for the purpose of advecting the tracers. Therefore we have formally included the continuity constraint (7) into the second subproblem, which is further referred to as the thermodynamical part of the model for convenience.

The vertical velocity is integrated from the ocean surface with kinematic boundary condition:

$$w = -F_\zeta \quad \text{on } \Gamma_1. \tag{10}$$

Because of (2) it also obeys the second boundary condition at the bottom:

$$w = 0 \quad \text{on } \Gamma_2. \tag{11}$$

Tracer evolution equations (8) are solved with the boundary conditions

$$K_v^m \partial_z C^m = q^m \quad \text{on } \Gamma_1, \tag{12}$$

$$(\nabla C^m, \partial_z C^m) \cdot \mathbf{n}_3 = 0 \quad \text{on } \Gamma_2 \cup \Gamma_4, \tag{13}$$

$$C^m = C_n^m \quad \text{on } \Gamma_3, \tag{14}$$

where q^m are the surface fluxes of the mth tracer, $\mathbf{n}_3$ is the 3d unit vector normal to the ocean bottom and C_n^m is a given distribution of the mth tracer at the open boundary.

2.2. Weak formulation of the problem

Let $H^1(\Omega)$ be the Sobolev space of functions in the square integrable space $L^2(\Omega)$, whose first derivatives also belong to $L^2(\Omega)$. Let $\mathbf{v}$ be in a subspace of $\mathbf{H}_0^1(\Omega) \equiv H^1(\Omega) \times H^1(\Omega)$ such that $\mathbf{v} = 0$ on the Dirichlet boundaries $\Gamma_2 \cup \Gamma_3 \cup \Gamma_4$, $\mathbf{u} = \mathbf{v} + \mathbf{v}_\gamma$ and $\mathbf{v}_\gamma$ is a sufficiently smooth extension of $u_n\mathbf{n}$ from Γ_3 onto Ω. The function $\mathbf{v}_\gamma$ is chosen in such a way that it vanishes on $\Gamma_2 \cup \Gamma_4$, satisfies (6) on Γ_3 and has zero vertical derivative at the surface. Using the above conventions and the notation $\mathbf{Lu} = f(\mathbf{k} \times \mathbf{u}) - \nabla A_l \cdot \nabla \mathbf{u} - \partial_z A_v \partial_z \mathbf{u}$, the differential formulation of (1) and (2) can be rewritten as

$$\mathbf{Lv} + g\nabla\zeta = \mathbf{F}_u - \frac{1}{\rho_0}\nabla p_\rho - \mathbf{Lv}_\gamma, \tag{15}$$

$$\mathscr{I}\nabla \cdot \mathbf{v} = F_\zeta - \mathscr{I}\nabla \cdot \mathbf{v}_\gamma, \tag{16}$$

where $\mathscr{I}$ is the vertical integration operator. For the purpose of convenience we shall refer to the relationships (15) and (16) as $\mathscr{L}X = \mathscr{G}$, where $X \equiv \{\mathbf{v}, \zeta\}$ belongs to $\mathbf{V} \equiv \mathbf{H}_0^1(\Omega) \times H^1(\Gamma_1)$ and $\mathscr{G} \equiv \{\mathbf{F}_u - (1/\rho_0)\nabla p_\rho - \mathbf{Lv}_\gamma; F_\zeta - \mathscr{I}\nabla \cdot \mathbf{v}_\gamma\}$.

To define a weak solution of (15) and (16) we require orthogonality of the residual $\mathscr{L}X - \mathscr{G}$ to any function $\widetilde{X}$ from $\mathbf{V}$ with respect to the scalar product

$$X \cdot \widetilde{X} \equiv \int_\Omega \mathbf{v}\tilde{\mathbf{v}}\,\mathrm{d}\Omega + \int_{\Gamma_1} \zeta g \tilde{\zeta}\,\mathrm{d}\gamma_1. \tag{17}$$

In other words we have to find $X \in \mathbf{V}$ such that

$$\mathscr{A}(X, \widetilde{X}) - \mathscr{R}(\widetilde{X}) = 0, \quad \forall \widetilde{X} \in \mathbf{V}, \tag{18}$$

where the bilinear form $\mathscr{A}$ and the linear functional $\mathscr{R}$ can be written down as follows:

$$\mathscr{A}(X, \widetilde{X}) \equiv \int_\Omega \left\{[f(\mathbf{k} \times \mathbf{v}) + g\nabla\zeta]\tilde{\mathbf{v}} + \nabla\mathbf{v}A_l\nabla\tilde{\mathbf{v}} + \partial_z\mathbf{v}A_v\partial_z\tilde{\mathbf{v}} - g\mathbf{v}\nabla\tilde{\zeta}\right\}\mathrm{d}\Omega, \tag{19}$$

$$\mathscr{R}(\widetilde{X}) \equiv -\mathscr{A}(X_\gamma, \widetilde{X}) + \{\mathbf{F}_u, F_\zeta\} \cdot \widetilde{X} + \int_{\Gamma_1} \boldsymbol{\tau}\tilde{\mathbf{v}}\,\mathrm{d}\gamma_1 - \int_\Omega \frac{1}{\rho_0}\nabla p_\rho \tilde{\mathbf{v}}\,\mathrm{d}\Omega - \int_{\Gamma_3} g\mathbf{v}_\gamma \mathbf{n}\tilde{\zeta}\,\mathrm{d}\gamma_3. \tag{20}$$

In the definition of $\mathscr{A}(X, \widetilde{X})$ we take into account that we work in the space of functions whose first derivatives are just square integrable and take the advantage of zero boundary values of $\mathbf{v}$ and $\tilde{\mathbf{v}}$. Relationships (18)–(20) represent the constrained momentum balance (1) and (2) in the form suitable for further FE discretization.

Weak formulation of the thermodynamical part of the model is similar to that of the momentum equations. Let C_γ^m be a sufficiently smooth extension from Γ_3 onto Ω of the function C_n^m specifying non-homogeneous Dirichlet boundary conditions (14), such that the normal derivatives of C^m_γ vanish on the boundaries $\Gamma_2 \cup \Gamma_3 \cup \Gamma_4$. Then the solution of the weak problem is a function $C^m \in \mathrm{H}^1_0$ taking zero values on Γ_3, such that

$$\mathscr{C}(C^m, \widetilde{C}^m) - \mathscr{R}_c(\widetilde{C}^m) = 0, \quad \forall \widetilde{C}^m \in \mathrm{H}^1_0. \tag{21}$$

The bilinear form $\mathscr{C}(C^m, \widetilde{C}^m)$ and the linear functional $\mathscr{R}_c(\widetilde{C}^m)$ are defined as follows:

$$\mathscr{C}(C^m, \widetilde{C}^m) = \int_\Omega \left\{ (\mathbf{u} \cdot \nabla C^m + w \partial_z C^m)\widetilde{C}^m + \nabla C^m K_l \nabla \widetilde{C}^m + \partial_z C^m K_v \partial_z \widetilde{C}^m \right\} \mathrm{d}\Omega, \tag{22}$$

$$\mathscr{R}_c(\widetilde{C}^m) = -\mathscr{C}(C^m_\gamma, \widetilde{C}^m) + \int_{\Gamma_1} q^m \widetilde{C}^m \, \mathrm{d}\gamma_1. \tag{23}$$

2.3. Finite-element discretization

In the present study we employ piecewise linear functions for local representation of both velocity and pressure in the momentum balance (the so-called P_1–P_1 pair). This choice was made because the use of higher-order FEs may generate spurious numerical modes which affect accuracy and stability of the numerical scheme. At the same time P_1–P_1 approximation is computationally efficient and was recently shown to be among the most accurate pairs in representing the geostrophic balance (Le Roux et al., 1998). To satisfy the LBB condition we employ the RFBF stabilization technique (Brezzi et al., 1996a,b) which may be considered as a universal recipe for avoiding spurious pressure modes and numerical instabilities associated with inadequate spatial resolution. An advantage of the RFBF approach is that the method provides control over the accuracy of FE schemes and in some cases gives an opportunity to obtain *exact* solutions of the original equations (Franca and Russo, 1997). The major idea of the RFBF stabilization is to enrich the approximation function space $\mathbf{V}$ with the "bubble functions" $\mathbf{v}_b \in \mathbf{V}_b$ which have zero values on the boundaries of the elements but contribute to the system matrix through their projections on the original basis functions. In the so-called pseudo-RFBF approach projections of the RFBFs are approximately assessed within every element of the mesh to eliminate the elementwise residuals of the Galerkin approximation (see Appendix A).

The utilized 3d FE mesh has nodes aligned in the vertical direction. For oceanic basins such a mesh can be generated as follows. First we construct unstructured triangulation of the sea surface $\mathscr{T}_{\Gamma_1}$ (Fig. 1). Vertical planes passing through the sides of the triangles $\mathscr{T}_{\Gamma_1}$ divide the domain into vertical water columns with lower faces forming the triangulation of the ocean bottom. Next we divide the ocean into a set of layers of horizontally variable thickness. Intersections of the layers and columns produce triangular prisms whose upper and lower faces are not necessarily parallel. The prisms are subdivided into three tetrahedra (two or one tetrahedron if one or two vertical edges of the prism vanish due to the slopes of layer interfaces). All the nodes of the resulting tetrahedral partition $\mathscr{T}_\Omega$ are located on the vertical lines passing through the nodes of $\mathscr{T}_{\Gamma_1}$.

Since geostrophy and hydrostatics are the major dynamical balances of the model, we did not displace the node layers far from the surfaces of constant gravity. Exceptions are made, however, near the ocean floor. In an attempt to resolve the bottom boundary layer we introduced a layer of elements with high vertical resolution following the bottom topography (Fig. 2).

In formulating the discrete version of (18)–(20) we assume that velocity is described by the elements of the finite-dimensional space $\mathbf{U}_{l,0}$ of continuous piecewise linear vector-valued func-

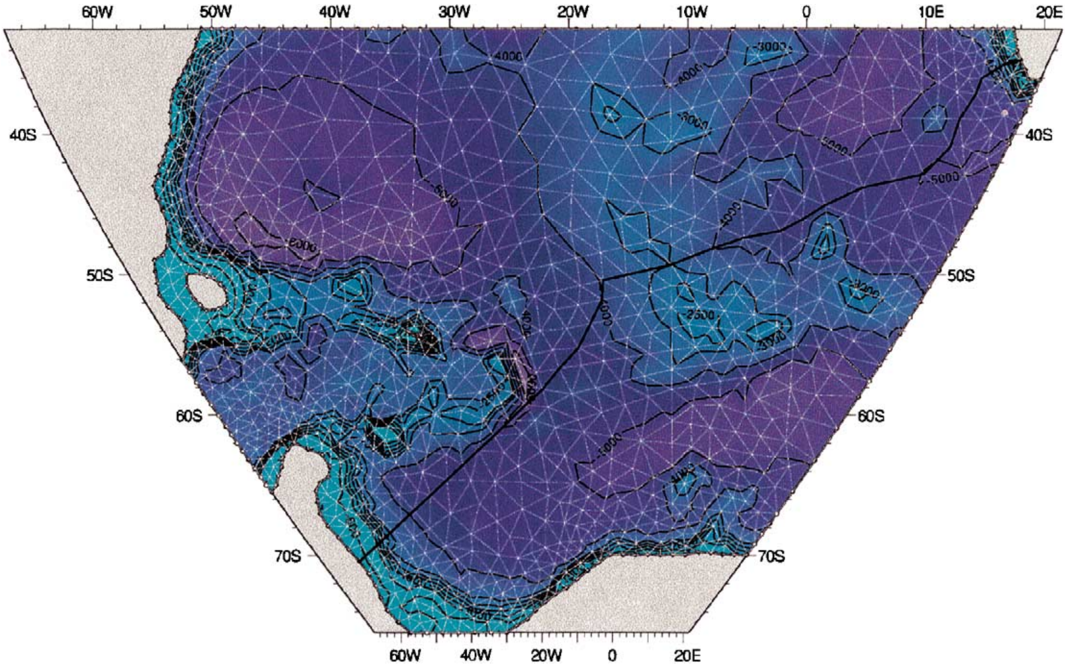

Fig. 1. Triangulation of the ocean surface superimposed on bottom topography. Solid line is the path of the vertical section shown in Fig. 2.

tions $\mathbf{v}_l$ defined on the partition $\mathscr{T}_\Omega$ and taking zero values on Dirichlet boundaries $\mathscr{T}_{\Gamma_i}$ $i = 2, \ldots, 4$. Sea surface height ζ is described by the space P_l of continuous piecewise linear functions ζ_l on $\mathscr{T}_{\Gamma_1}$. The set of "forcing functions" $\boldsymbol{\tau}$, p_ρ, $\mathbf{F}_u$ and F_ζ is also restricted to piecewise linears: $\boldsymbol{\tau} \in P_l \times P_l$, $p_\rho \in \mathbf{U}_l$, $\mathbf{F}_u \in \mathbf{U}_l$ and $F_\zeta \in P_l$.

Following the BF technique for the problems with constraints (e.g. Pierre, 1995; Franca and Russo, 1996a, in relation to Stokes problem) we enrich with the BF the velocity subspace only. Let the augmented space be $\mathbf{V}_h \equiv \mathbf{V}_l \times \mathbf{V}_b$. Given that, the stabilized restriction of (18)–(20) to $\mathbf{V}_h \times P_l$ can be written down in the form:

$$\mathscr{A}(X_l, \widetilde{X}_l) - \mathscr{R}(\widetilde{X}_l) + \sum_{k=1}^{K} (\mathbf{v}_b \cdot \mathscr{L}^\dagger \widetilde{X}_l)_k = 0 \quad \forall \widetilde{X}_l \in \mathbf{U}_{l,0} \times P_l, \tag{24}$$

where summation is taken over all tetrahedra T_k, $k = 1, \ldots, K$ of the FE mesh, and $\mathscr{L}^\dagger$ is the adjoint of $\mathscr{L}$ in T_k. Under certain simplifying assumptions the scalar products in (24) can be expressed in terms of the elementwise projections of the residuals

$$\mathbf{r} = \mathbf{L}\mathbf{v}_l + g\nabla\zeta_l - \mathbf{F}_u + \frac{1}{\rho_0}\nabla p_\rho + \mathbf{L}\mathbf{v}_\gamma \tag{25}$$

onto $\mathscr{L}^\dagger \widetilde{X}_l$, so that

$$(\mathbf{v}_b \cdot \mathscr{L}^\dagger \widetilde{X}_l)_k = \Big([-\varepsilon_1^k \mathbf{r} + \varepsilon_2^k \mathbf{k} \times \mathbf{r}] \cdot \mathscr{L}^\dagger \widetilde{X}_l \Big)_k, \tag{26}$$

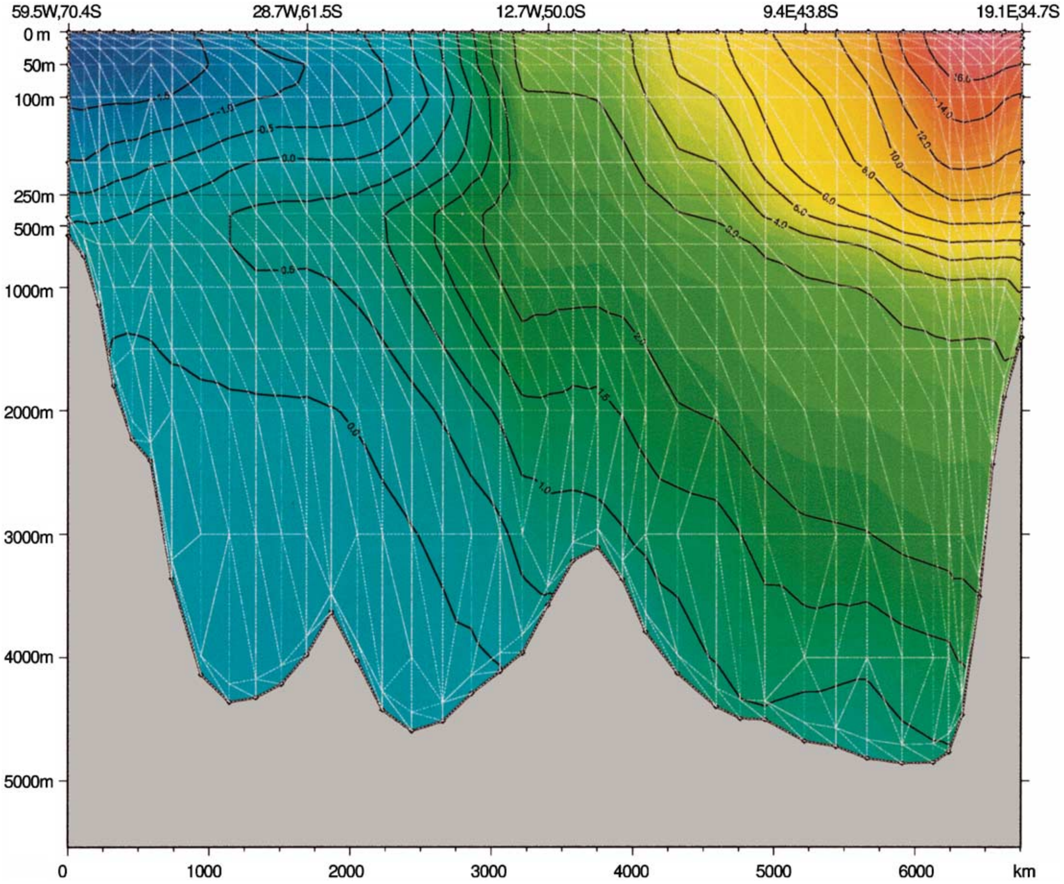

Fig. 2. The vertical structure of the mesh superimposed on the temperature field from the Southern Ocean Hydrographic Atlas of Olbers et al. (1992). Contour interval is 0.5 °C.

where $\varepsilon^k_{1,2}$ are the certain constants depending upon the structure of the dynamical operator within an element. A derivation of (26) is given in the next section for a simplified case. More details can be found in Appendices A and B, where the general ideas of the BF method are outlined.

Relationships (24)–(26) represent the stabilized version of the constrained momentum balance problem (18)–(20) restricted to the finite-dimensional space $\mathbf{V}_l \times P_l$. The weak problem (24)–(26) is solved following the standard Galerkin technique: after introducing a conventional set of linear basis functions within the elements T_k we perform elementwise integrations by quadrature formulae and obtain representation of (24) in the space of nodal values of $X_l, \widetilde{X}_l$. Partial differentiation with respect to the nodal values of $\widetilde{X}_l$, yields a set of linear equations which is then solved to obtain the unknown vector of nodal values of X.

Discretization of the weak formulation of the thermodynamical part of the model is analogous to that of the momentum. We approximate tracer concentrations C^m by the piecewise linear functions $C^m_l \in \mathbf{U}_0$ defined on the same tetrahedral partition $\mathscr{T}_\Omega$. To stabilize the FE scheme for the problem (21) $\mathbf{U}_0$ is augmented with BFs yielding the stabilized problem of the form:

$$\mathscr{C}(C_l^m, \widetilde{C}_l^m) + \sum_{k=1}^{K} \int_{T_k} C_b^k \mathscr{L}_c^\dagger \widetilde{C}_l^m \, \mathrm{d}\Omega - \mathscr{R}_c(\widetilde{C}_l^m) = 0, \tag{27}$$

where $\mathscr{L}_c^\dagger$ is the adjoint to the operator $\mathscr{L}_c = \mathbf{u} \cdot \nabla + w\partial_z - \nabla \cdot K_l \nabla - \partial_z K_v \partial_z$ on the element T_k.

The key point of the approximation of (27) is the choice of the space of functions for the representation of the velocities which advect the tracer. This choice defines the dimension and shape of tracer BFs and consequently the form of the stabilization terms.

In the present work we utilize piecewise constant velocities $\mathbf{u}_c$, w_c for tracer advection. Our choice is motivated by the following three reasons. First of all, this set of 3d velocities is non-divergent within each element, which leads to the essential simplification of the stabilization scheme. For piecewise constant velocities the optimal space of bubbles contains only one BF per element corresponding to the constant distribution of the residuals on the element. Second, if the tracer concentration is represented by linears and the advecting velocity by piecewise constant velocities the RFBF stabilization is equivalent to the well-known "stream-line diffusion" scheme. Finally, for the piecewise constant velocities we can easily define the algorithms for projecting the horizontal velocities $\mathbf{u}_l + \mathbf{u}_b \rightarrow \mathbf{u}_c$ and for computing w_c which obey the integral constraints of volume and tracer conservation.

We do not discuss derivation of stream-line diffusion scheme but refer the reader to the original papers (e.g. Franca and Russo, 1996b). A detailed description of the algorithm for obtaining of 3d velocities $(\mathbf{u}_c, w_c)$ can be found in Appendices A and B.

2.4. Details of the numerics

Density and baroclinic pressure anomalies ρ, p_ρ are approximated by piecewise linears. The equation of state (9) is applied to the nodal values of temperature and salinity. The resulting value of density is prescribed to the corresponding nodal value of $\rho \in U_l$. Integration of (3) is then performed analytically along each vertical line of the nodes. The baroclinic pressure anomaly $p_\rho \in U_l$ is specified by simply extracting the nodal values of p_ρ obtained after integration. The means over Ω are subtracted from the fields ρ and p_ρ prior to any further calculations. Diffusion and metric coefficients are represented by piecewise constant functions in both the dynamical and thermodynamical parts of the model.

The FE model code assembles system matrices, calculates the right-hand side vectors and solves the sets of linear equations corresponding to dynamical and thermodynamical equations. The matrices are assembled and stored in a full sparse column format. The systems of linear equations are solved using the SITRSOL routine of the Scientific Fortran Library (Cray) which is a numerical realization of the generalized minimum residual algorithm (Saad, 1993) with preconditioning based upon the truncated least-squares polynomial expansion of degree 2.

3. Applications to idealized problems

In this section we show some of the model testing results with an intention to demonstrate its performance and to provide a somewhat more detailed insight into the RFBF technique.

3.1. Stabilization scheme for the Ekman problem

The equations of classical Ekman problem follow from Eqs. (1)–(6) for horizontally homogeneous flows:

$$f(\mathbf{k}\times\mathbf{u}) - \partial_z(A_v\partial_z\mathbf{u}) = 0, \tag{28}$$

$$A_v\partial_z\mathbf{u}(\Gamma_1) = \boldsymbol{\tau}, \quad \mathbf{u}(\Gamma_2) = 0. \tag{29}$$

The BF-stabilized FE formulation of (28), (29) can be written as: find $\mathbf{v}_h \in \mathbf{V}_h$, such that

$$\int_\Omega \{f(\mathbf{k}\times\mathbf{v}_h)\tilde{\mathbf{v}}_h + \partial_z\mathbf{v}_h A_v\partial_z\tilde{\mathbf{v}}_h\}\,\mathrm{d}\Omega - \int_{\Gamma_1}\boldsymbol{\tau}\tilde{\mathbf{v}}_h\,\mathrm{d}\gamma_1 = 0, \quad \forall\tilde{\mathbf{v}}_h \in \mathbf{V}_h. \tag{30}$$

The space $\mathbf{V}_h$ contains piecewise linear functions $\mathbf{v}_l$ defined on the partition $\mathscr{T}_\Omega$, and satisfying $\mathbf{v}_l(z=-H)=0$ and bubble functions $\mathbf{v}_b^k$ with support T_k, $k=1,\dots,K$, such that $\mathbf{v}_h \equiv \mathbf{v}_l + \mathbf{v}_b$. Since the coefficients f and A_v are defined as elementwise constants, the viscous term $\partial_z(A_v\partial_z\mathbf{v}_l)$ is zero within an element and the residuals $\mathbf{r}^k = f\mathbf{k}\times\mathbf{v}_l$ are linear functions in T_k. This means that RFBFs with only four degrees of freedom (two for every velocity component) are required to eliminate the residuals on each element. Although we can easily build the RF FE solution to (28) and (29), a suboptimal (pseudo-RFBF) scheme will be considered here to maintain similarity with discretization of the general problem.

We assume that BFs are spanned by just two orthogonal basis functions $\boldsymbol{\varphi}_b^1 = (\xi,\eta)$ and $\boldsymbol{\varphi}_b^2 = (-\eta,\xi)$, which satisfy the following boundary value problem:

$$-f\eta - \partial_z(A_v\partial_z\xi) = 1; \quad f\xi - \partial_z(A_v\partial_z\eta) = 0, \tag{31}$$

$$\xi(\partial T_k) = \eta(\partial T_k) = 0 \quad \forall T_k \tag{32}$$

and are used to eliminate the mean value of the residuals on each element T_k. The amplitudes of suboptimal BFs are found as a solution to the following weak problem (cf. (A.2) in Appendices A and B): find $\mathbf{v}_h \in \mathbf{V}_h$, such that

$$\int_{T_k}[f(\mathbf{k}\times\mathbf{v}_h^k) - \partial_z(A_v\partial_z\mathbf{v}_h^k)]\tilde{\mathbf{v}}_b^k\,\mathrm{d}z = 0 \quad \forall\tilde{\mathbf{v}}_b^k \in \mathrm{span}(\boldsymbol{\varphi}_\mathrm{b}^1,\boldsymbol{\varphi}_\mathrm{b}^2). \tag{33}$$

The problem (33) is solved by setting to zero partial derivatives of (33) with respect to the two unknown amplitudes of the expansion of $\tilde{\mathbf{v}}_b$ in $\boldsymbol{\varphi}_b^1, \boldsymbol{\varphi}_b^2$. After that the pseudo-RFBFs are substituted into (30) to obtain the final form of the stabilized Ekman problem in $\mathbf{V}_l$: find $\mathbf{v}_l \in \mathbf{V}_l$ such that

$$\int_\Omega \{f(\mathbf{k}\times\mathbf{v}_l)\tilde{\mathbf{v}}_l + \partial_z\mathbf{v}_l A_v\partial_z\tilde{\mathbf{v}}_l\}\,\mathrm{d}\Omega - \int_{\Gamma_1}\boldsymbol{\tau}\tilde{\mathbf{v}}_l\,\mathrm{d}\gamma_1 + \sum_{k=1}^{K} f^2\int_{T_k}[\varepsilon_1^k(\mathbf{k}\times\mathbf{v}_l) + \varepsilon_2^k\mathbf{v}_l](\mathbf{k}\times\tilde{\mathbf{v}}_l)\,\mathrm{d}z = 0,$$

$$\forall\tilde{\mathbf{v}}_l \in \mathbf{V}_l, \tag{34}$$

where

$$\varepsilon_1^k = \frac{c}{|f|}\frac{s_k}{s_k^2+1}, \quad \varepsilon_2^k = \frac{cf}{f^2}\frac{1}{s_k^2+1}, \tag{35}$$

c is the normalization constant, and

$$s_k = \left[A_v \int_{T_k} (\partial_z\xi)^2 + (\partial_z\eta)^2 \, \mathrm{d}z\right]\left[|f| \int_{T_k} (\xi^2 + \eta^2) \, \mathrm{d}z\right]^{-1}.$$

The non-dimensional parameter s_k varies from one element to another due to variation of the mesh Ekman number $E = (2A_v/|f|h_k^2)^{1/2}$ (h_k is an element diameter). Since the use of the analytical expression for $s_k = s_k(E)$ in a numerical scheme is inefficient, we utilize the approximation

$$s_k = \begin{cases} 5.0E^2, & \text{if } E > 0.6 \\ 0.063 + 4.83E^2, & \text{if } 0.1 < E \leqslant 0.6 \\ E + 1.12E^2, & \text{if } E \leqslant 0.1 \end{cases} \tag{36}$$

which fits the precise formula within 3% in the interval of E variation, typical for oceanic conditions.

The stabilization scheme (34) will be referred to as BM hereafter. Standard Galerkin scheme GM can be obtained from BM by setting to zero the stabilization weights ε_1, ε_2. In both BM and GM schemes the boundary condition on Γ_1 is represented by the same surface integral. Note that BM stabilization does not affect the approximation of non-homogeneous Newman boundary condition because $\mathbf{v}_b$ vanish on Γ_1 by definition. When the mesh Ekman number is small this shortcoming invokes high amplitudes of the bubble functions in the boundary layer element, which may may distort the pseudo-RFBF solution. A natural way to deal with that problem is to convert the original surface integral in (30) into the volume integral by introducing an analogue of the δ-function so that the bubble functions in the elements adjacent to the surface will have non-zero projection onto the surface forcing.

Straightforward computations show that in this case stabilization part of (34) is augmented by the term:

$$\sum_{k=1}^{K} f \int_{T_k} \delta_k[-\varepsilon_1^k \boldsymbol{\tau}_l + \varepsilon_2^k(\mathbf{k} \times \boldsymbol{\tau}_l)](\mathbf{k} \times \tilde{\mathbf{v}}_l) \, \mathrm{d}z,$$

where δ_k is not zero only for the elements T_k intersecting with Γ_1. For those elements δ_k can be expressed in terms of the local linear basis functions ϕ_l^i as $\delta_k = \int_{\partial T_k} \phi_l^i \phi_l^j \, \mathrm{d}\gamma_1 / \int_{T_k} \phi_l^i \phi_l^j \, \mathrm{d}\Omega$. This modification of the pseudo-RFBF scheme will be referred to as MBM.

In the numerical tests we solved (28) and (29) with the unit forcing $\boldsymbol{\tau} = (1, 0)$ on a homogeneous grid consisting of $K = 25$ elements (26 nodes). The computations were done for various values of E using the GM, BM and MBM schemes. Fig. 3 summarizes the results of the FE testing of the Ekman problem.

Errors ϵ of the FE solutions with respect to the analytical Ekman spiral are measured in two ways: as the rms of the nodal value differences ϵ_l and as the rms of the elementwise integrals of the differences between these solutions ϵ_c. Both errors are normalized by the corresponding amplitudes of the analytical solution $\mathbf{v}^t$:

$$\epsilon_l = \left\{ \frac{\sum_{i=1}^{K+1} (\mathbf{v}_h(z_i) - \mathbf{v}^t(z_i))^2}{\sum_{k=1}^{K+1} (\mathbf{v}^t(z_i))^2} \right\}^{1/2}; \quad \epsilon_c = \left\{ \frac{\sum_{k=1}^{K} [\int_{T_k} (\mathbf{v}_h - \mathbf{v}^t) \, \mathrm{d}z]^2}{\sum_{k=1}^{K} [\int_{T_k} (\mathbf{v}^t) \, \mathrm{d}z]^2} \right\}^{1/2}.$$

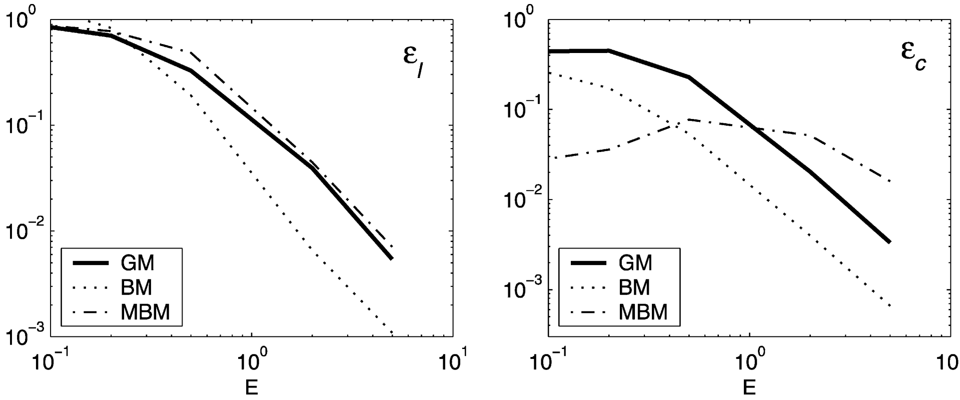

Fig. 3. Errors ϵ_l and ϵ_c as functions of the Ekman number E for the standard Galerkin (GM), pseudo-RFBF (BM) and modified bubble function (MBM) methods.

The integral norm ϵ_c measures the errors in the projective subspace of elementwise constant functions $\mathbf{V}_c$ (the projection takes into account the BF part of the BM and MBM solutions, see Appendices A and B, Eq. (A.6)), while the "pointwise norm" ϵ_l is an error estimate in $\mathbf{V}_l$ (since the BFs vanish in nodal points ϵ_l represents only the linear part of the FE solutions).

Numerically, RFBF method should give the exact analytical values in the nodes ($\epsilon_l = 0$). This is not the case since we utilize suboptimal (pseudo-RF) bubble functions. Nevertheless, the results of the BM method are superior to GM at $E > 0.2$. Note that at $E < 0.5$ the analytical solution is effectively zero outside the element adjacent to the sea surface $z = 0$.

With the decrease of E the bubble part of the stabilized BM solution becomes large, causing a considerable growth of ϵ_l due to the increasing role of fast varying components in the analytical solution which are not described by suboptimal bubbles. Note that ϵ_l (MBM) does not grow as fast as ϵ_l (BM), being quite close to ϵ_l (GM). We attribute that to the additional stabilization of the surface forcing which reduces the amplitude of $\mathbf{v}_b$ together with the "suboptimality" errors caused by truncation of the optimal basis in $\mathbf{V}_b$.

In oceanographic applications it is important for a FE approximation to provide not only the reasonable nodal values of the solution at $E < 1$ but also correct Ekman boundary layer widths and transports. In that sense ϵ_l does not seem to be a good indicator of the quality of the numerical solution at small E: fast variation of the analytical solution within the near-surface element can be associated with large integral errors ϵ_c while having a formally small value of ϵ_l. Pseudo-RFBF method effectively removes the integral errors (measured in terms of ϵ_c), whereas the standard Galerkin technique does not treat these errors separately and performs much worse in the sense of the ϵ_c error (Fig. 3). At $E < 0.5$ the ϵ_c error of the stabilized solutions is always several times smaller than the GM error. Note that the ϵ_c (MBM) does not grow at small E and remains reasonably low in the entire range of E variation.

In the 3d ocean circulation model we utilize the MBM method. This method provides almost the same nodal errors as GM solution in the entire range of E. Although MBM technique results in somewhat larger ϵ_c errors at $E > 0.5$ because of the approximation error of the surface integral by volume integral, these errors are still at an acceptable level within the entire range of E. An important advantage of the MBM scheme is the weak dependence of ϵ_c on E and the relatively small amplitude of bubble constituent of the solution within the wide range of parameters. The latter property is important from the numerical point of view because of the suboptimality of the BF basis used in this study.

3.2. Stabilized solution of the steady state shallow water equations

The original 3d problem (15) and (16) can be reduced to the variational setting of the shallow water equations under the assumption of vertical homogeneity of all the 3d fields. In this case the weak problem for 2d velocities $\mathbf{v}(\lambda,\varphi)$ and sea surface elevation $\zeta(\lambda,\varphi)$ reads: find $X \equiv \{\mathbf{v},\zeta\} \in \mathbf{V}$ and $\widetilde{X} \in \mathbf{V}$, such that

$$\int_\Omega \{f(\mathbf{k}\times\mathbf{v})\tilde{\mathbf{v}} + g\nabla\zeta\tilde{\mathbf{v}} + \nabla\mathbf{v}A_l\nabla\tilde{\mathbf{v}} - g\mathbf{v}\nabla\tilde{\zeta}_l - \mathbf{F}_\mathbf{v}\tilde{\mathbf{v}}\}\,\mathrm{d}\Omega = 0, \quad \forall\widetilde{X}\in\mathbf{V}, \tag{37}$$

where $\mathrm{d}\Omega = R^2 H\cos\varphi\,\mathrm{d}\lambda\,\mathrm{d}\varphi$, $H(\lambda,\varphi)$ is the ocean depth, $\mathbf{F_u}$ is the mass forcing vector and λ, φ are the spherical coordinates. We consider a rectangular domain Ω with homogeneous Dirichlet boundary conditions $\mathbf{v}=0$ at $\partial\Omega$. The weak problem (37) corresponds to the differential formulation

$$f(\mathbf{k}\times H\mathbf{v}) + gH\nabla\zeta - \nabla(HA_l\nabla\mathbf{v}) - H\mathbf{F}_\mathbf{v} = 0, \tag{38}$$

$$\nabla(H\mathbf{v}) = 0, \tag{39}$$

$$\mathbf{v}(\partial\Omega) = 0. \tag{40}$$

To discretize (37) we introduce a partition of Ω as a set of triangles T_k, $k=1,\dots,K$, while the FE functional spaces are defined as $\mathbf{V}_h = \mathbf{V}_l\times\mathbf{V}_b$ and P_l where subscript l denotes spaces of continuous elementwise linear functions in T_k and $\mathbf{V}_b$ is the space of bubble functions. Stabilization weights $\epsilon^k_{1,2}$ are calculated using the expressions analogous to those derived in the previous section, with the mesh Ekman number $E = (2A_l/|f|h_k^2)^{1/2}$.

The RFBF approximation was tested against the analytical solution of (38)–(40) in a rectangular basin on a sphere $\lambda=(0,L_\lambda)$, $\varphi=(0,L_\varphi)$ composed of 384 triangles. Vertices of the triangles formed a homogeneous $17^\circ\times13^\circ$ grid so that the dimension M of the system matrix was $17\times13\times3=663$.

The analytical velocity field $\mathbf{u}=(u,v)$ satisfying (38)–(40) was prescribed by defining the total transport stream function Ψ:

$$\Psi = \Psi_0\sin^2(\pi\lambda/L_\lambda)\sin^2(\pi\varphi/L_\varphi), \quad H\mathbf{u} = \mathbf{k}\times(\nabla\Psi).$$

Bottom topography and the Coriolis parameter were specified by

$$H(\lambda,\varphi) = H_0 + H_1\sin(\pi\lambda/L_\lambda)\sin(\pi\varphi/L_\varphi), \quad f = 2\omega\sin\varphi_0,$$

with $H_0=300$ and $H_1=2700$ m respectively. The analytical surface elevation ζ was defined by the linear and quadratic functions of λ and φ, whose amplitudes are chosen in a way that $\|g\nabla\zeta\|\approx\|f\mathbf{u}\|$ for $E<1$ and $\|g\nabla\zeta\|\approx\|\nabla A_l\nabla\mathbf{u}\|$ for $E>1$. After that $\mathbf{F_u}$ was computed by direct substitution of $\mathbf{u}$ and ζ into (38). Given that forcing we reconstructed $\mathbf{v}$ and ζ using the FE model.

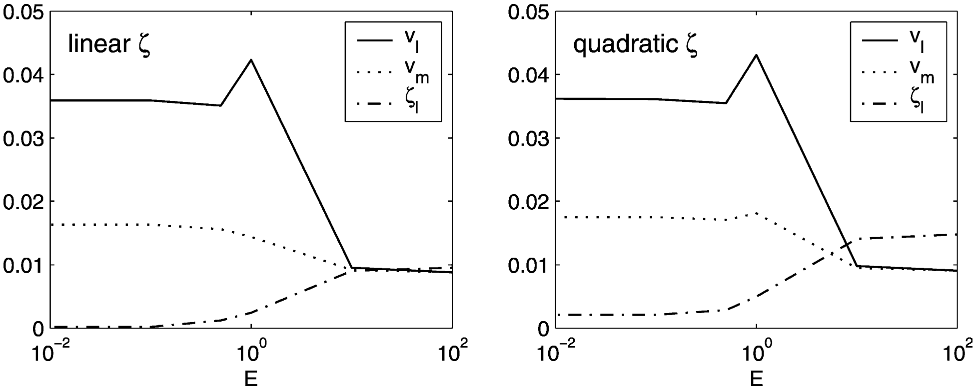

Fig. 4. Errors of the pseudo-RFBF stabilized FE solution to the shallow water equations for the forcing functions $\mathbf{F_u}$ which correspond to linear and quadratic variation of ζ across the domain.

The parameters φ_0 and A_l were varied to study sensitivity of the approximation to the mesh Ekman number E. Following the discussion in the previous section, we compare functions from different spaces by projecting them onto $\mathbf{V}_l$. BFs were projected using the the following weak problem: find $\mathbf{v}_{bl} \in \mathbf{V}_l$ such that

$$\int_\Omega \mathbf{v}_b l \tilde{\mathbf{v}}_l \,\mathrm{d}\Omega = \sum_{k=1}^{K} \int_{T_k} [\epsilon_1^k \mathbf{r}^k - (\epsilon_2^k \mathbf{k} \times \mathbf{r}^k)] \tilde{\mathbf{v}}_l \,\mathrm{d}\Omega, \quad \forall \tilde{\mathbf{v}}_l \in \mathbf{V}_l. \tag{41}$$

The sum $\mathbf{v}_m = \mathbf{v}_l + \mathbf{v}_b l$ can be treated as a projection of the stabilized FE solutions on $\mathbf{V}_l$. To project the analytical solution we simply took the values of the corresponding functions at nodal points. The FE solution error was estimated as RMS of nodal differences between analytical and FE fields. It was then normalized by the RMS amplitude of the analytical solution at nodal points. Obviously, this error includes both the projection and approximation errors.

The results of the set of the experiments are presented in Fig. 4. They show that FE solution errors lie within the estimate of approximation error for the second-order schemes: $(h_k/L)^2 \approx 10^{-2}$ for the wide range of E. In cases when diffusion dominates over rotation (large E) the system matrix is better conditioned and the convergence is achieved in 50–55 iterations. But even in the worst case of $E = 0.01$ the number of iterations required for the solution did not exceed 114, that is acceptable regarding the large dimension of the system matrix.

Another set of experiments was made with varying the amplitude of $|\zeta|$ under fixed Ekman number $E = 0.1$. That was done to check the FE scheme's ability to separate the potential $\mathbf{F}_\mathbf{u}^\mathrm{p}$ and solenoidal $\mathbf{F}_\mathbf{u}^\mathrm{s}$ constituents of the forcing $\mathbf{F_u}$. In an ideal situation, only the solenoidal constituent should affect the velocity field. Results of these computations have shown that for $\kappa = |\mathbf{F}_\mathbf{u}^\mathrm{p}|/|\mathbf{F}_\mathbf{u}^\mathrm{s}| < 15$ the FE solution accuracy is kept within the error bars of the second-order schemes. For higher values of κ velocity errors grow proportionally to $|\zeta|$. We assume that a significant part of this growth is attributed to projection error of the analytical solution onto the nodes. In the case of linear surface elevations the corresponding threshold value of κ turned to be about 3 orders of magnitude larger than for quadratic ζ.

4. Circulation in the South Atlantic ocean

In order to assess the capability of the model to simulate density and wind driven flows, we considered simulations of the South Atlantic ocean between 67.5°W–21.5°E and 32.5°S–76.5°S (Fig. 1) Triangulation of the sea surface was performed by means of the 2d mesh generator `GEOMPACK` (Joe, 1991), which allows to control the mesh resolution via a nodal density function derived from bathymetry (NOAA, 1986). The rigid boundary of the domain is delineated along the 50 m isobath. Horizontal resolution of the tetrahedral mesh (Figs. 1 and 2) varies between 20 and 200 km. Vertical nodal levels are 0, 10, 25, 50, 100, 200, 400, 650, 1000, 1500, 2000, 3000, 4000, 5000, 6000 and 7000 m. There are $N = 70{,}822$ elements and 14,631 nodes.

We describe below three types of diagnostic computations. The first one is a classical problem of reconstruction of the 3d velocity field driven by the given wind and density distributions. Solution to this problem serves as a test for the momentum balance equations of the model. The second problem is computation of the of a steady state tracer distribution for a given velocity field and surface fluxes. The third type of diagnostic computation is a combination of the previous ones: given the surface fluxes, retrieve a steady state velocity and tracer distributions. This nonlinear problem is solved by the 3d variational data assimilation method which can be viewed as a least-squares optimization under the dynamical constraints imposed by the FE model equations. We consider the results of optimization as an objective test of the code which quantitatively assesses the model's ability to simultaneously fit a number of independent data sets within their error bars. The data sets used include long-term observations of the oceanic temperature and salinity, sea surface elevation and fluxes at the ocean surface.

4.1. Diagnostic simulations

To diagnose the large scale velocity field we forced the equations (1)–(3) by the annual mean wind stress data (Trenberth et al., 1989). The density field was taken from the Southern Ocean climatology (Olbers et al., 1992). Normal velocities at the open boundaries were calculated by the dynamical method. Momentum diffusion coefficients in the interior of the ocean were set to $A_l = 500$ m^2/s and $A_v = 0.0001$ m^2/s. Within the surface and bottom boundary layers we used higher values for A_v corresponding to the Ekman layer thickness of 10 and 25 m respectively. To simulate lateral boundary layers the magnitude of A_l has been increased up to three times within the elements adjacent to the rigid boundary.

The computed currents (Fig. 5) capture well the major circulation features of the South Atlantic and quantitatively correspond to the latest observations. For instance, total transports of the Faulkland, Agulhas and the Antarctic circumpolar currents (ACCs) are diagnosed as 60, 50 and 135 Sv respectively. These figures lie well within the limits of the corresponding estimates found in literature (e.g. Reid, 1989; Stutser and Krauss, 1998). The model also captures well such delicate feature as the latitude of the off-shore separation of the Brazil Current at 40°S near the coast of South America. The ACC seems to be oversmoothed owing to excessive filtering of the climatological density. At the same time the topographically controlled path of ACC east of the Drake Passage is captured well. The Weddell Gyre, although clearly visible south of 65°S, appears to be less realistic as a result of sparseness of the hydrological data which underlie climatology in that region. At the open boundaries of the domain one can observe a strong artificial divergence of the

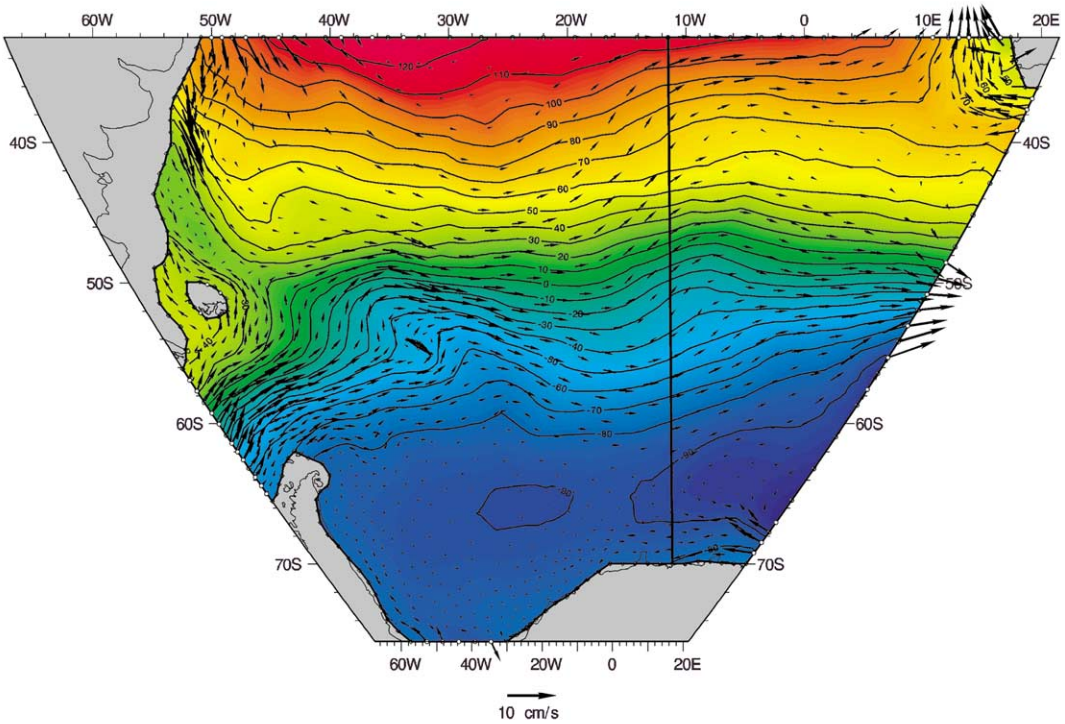

Fig. 5. Vertically averaged velocities and sea surface height diagnosed without data assimilation. Contour interval is 10 cm. Solid line shows the location of the vertical section presented in Figs. 4 and 5.

horizontal flow (51°S, 20°E; 30°S, 15°E) which indicates inconsistency between our guess for the normal velocities at the open boundaries and the forcing inside the domain.

Vertical structure of the velocity field (Fig. 6) is characterized by realistically thin Ekman layers and a weak eastward current near the Antarctic continental shelf. Two branches of ACC, separated by the Indo-Atlantic mid-ocean ridge, are also well captured. Vertical velocities (Fig. 7) exhibit strong downwelling near the Antarctic continent. In the model it is topographically induced by the Southern Ocean climatology, but in reality these motions may be forced by coastal cooling, which affects hydrology through dynamical teleconnections.

Diagnostic computations demonstrated a high computational efficiency of the model. Simulation of a steady state 3d circulation and sea surface elevation for a given density distribution and boundary forcing required about 53 s on Cray YMP. Computation of a steady state temperature and salinity distributions for a given velocity field and boundary conditions proved to be even more efficient, requiring approximately 12 s of CPU.

4.2. Optimization

To test the model against several types of climatological data a variational optimization scheme has been constructed. Such an approach becomes possible because FE formulation of the code provides a favorable environment for construction of the data assimilation schemes based on the

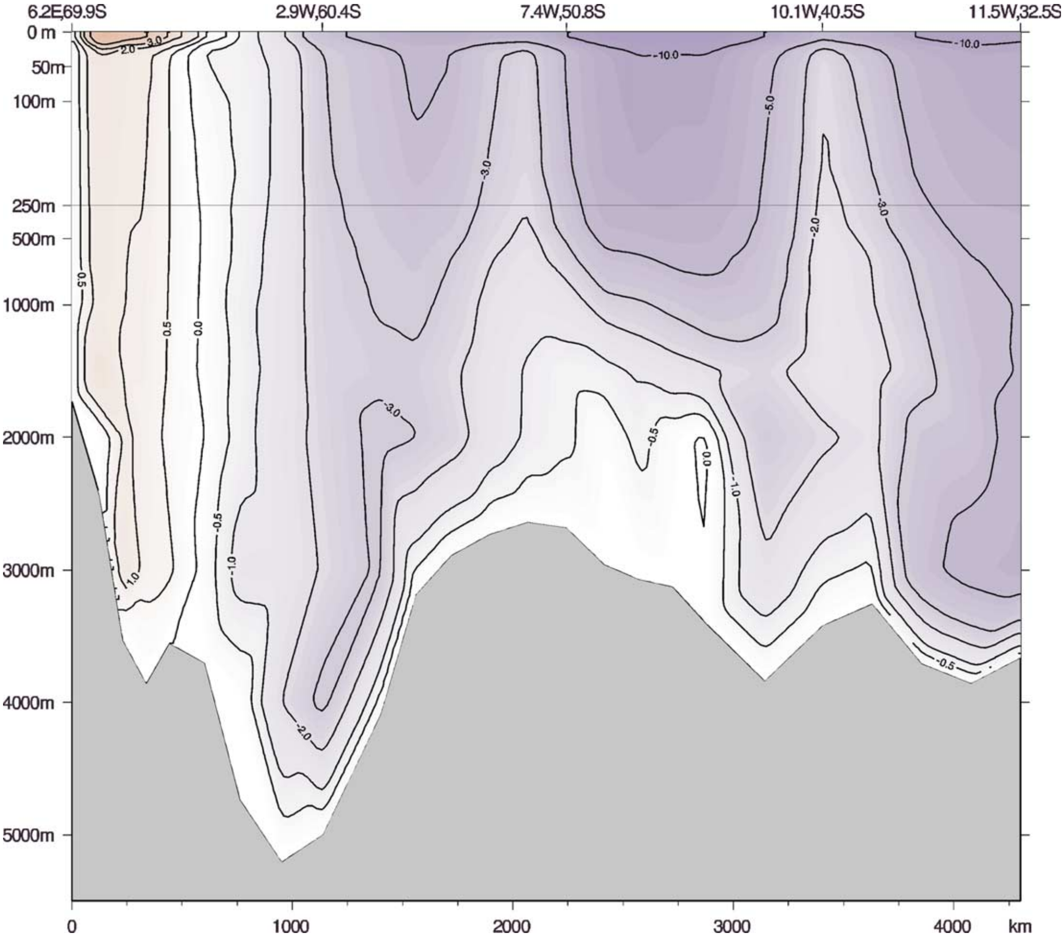

Fig. 6. Cross-section velocity at the vertical section (Fig. 5) diagnosed without data assimilation. Contour values are in cm/s.

adjoint equations. The latter are obtained by simple transposition of the system matrices explicitly present in the code. This property of the FE method enabled us to test the model against data at very low expense.

In constructing the optimization scheme we treat the dynamical part of the model as a strong constraint, while thermodynamics is treated in a weak form by introducing a Gaussian error ε_ρ into the buoyancy conservation equation. This error term accounts for the processes which were not explicitly included into the model. Momentum balance on the other hand is satisfied exactly. With this approach we do not solve the steady state equation for buoyancy conservation but calculate the residuals which are then eliminated in the course of optimization. That increases computational efficiency but expands the space of control variables which has to include density values in all nodal points as the parameters to be varied in search for a dynamically constrained minimum of the cost function $\mathscr{J}$. Therefore full list of the varied parameters (control variables) includes (i) density anomaly in all nodal points, (ii) wind stress values in all nodal points on Γ_1,

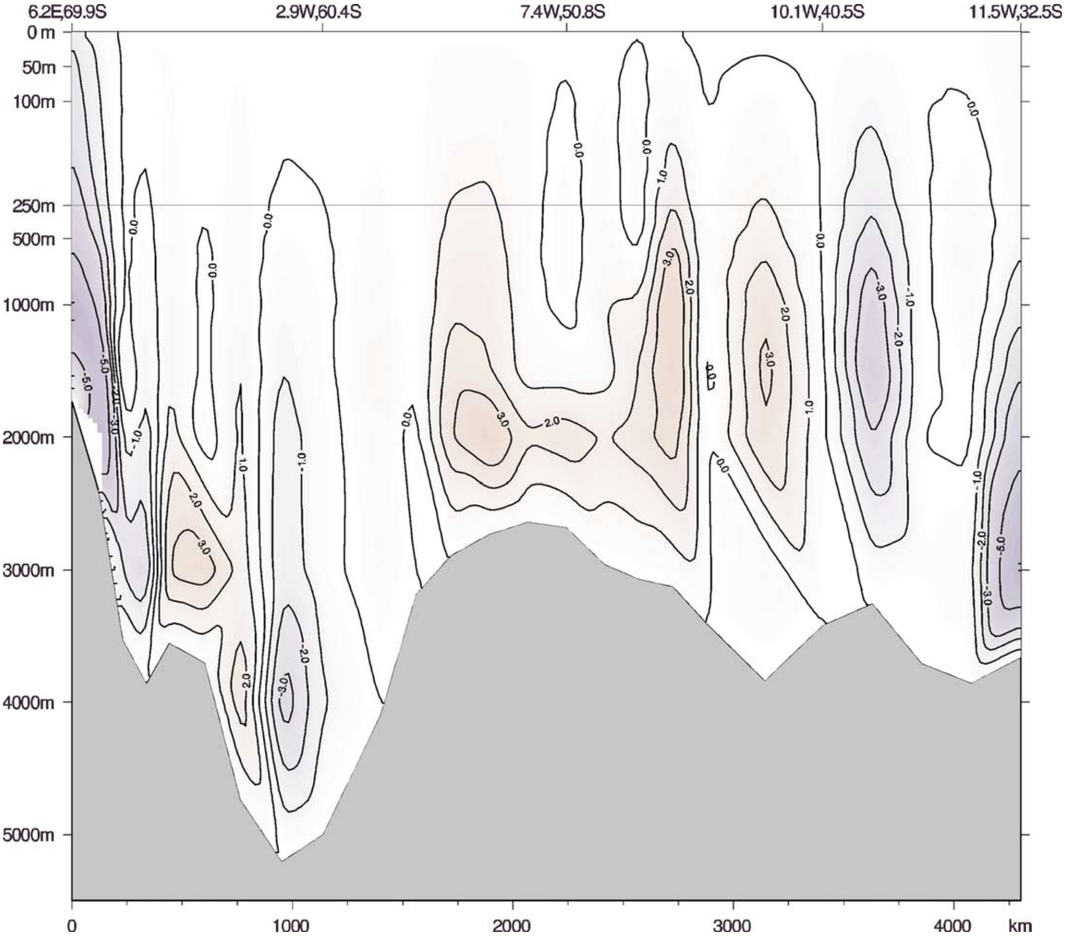

Fig. 7. Vertical velocity at the section (Fig. 5) diagnosed without data assimilation. Contour interval is 10^{-3} cm/s.

and (iii) normal velocity components in all open boundary nodes Γ_3. The total number of control variables is 16,893.

The cost function $\mathscr{J}$ which basically measures the magnitude of the model/data misfit can be treated as the argument of the Gaussian probability density function on the space of model solutions (Thacker, 1989). We assume that independent types of data are δ-correlated, so that $\mathscr{J}$ has the following structure:

$$\mathscr{J} = \left\{ \sum_{n=1}^{N} W_\rho(\mathbf{r},z)(\rho-\rho_n^*)^2 + \sum_{n=1}^{N_{\Gamma_1}} W_\tau(\boldsymbol{\tau}-\boldsymbol{\tau}_n^*)^2 + \sum_{i=1}^{I_s} W_u(\mathbf{U}_i\mathbf{n}-U_i^*)^2 + \sum_{n=1}^{N_\zeta} W_\zeta(\zeta-\zeta_n^*)^2 \right\}_{(\mathrm{I})} + \left\{ \sum_{n=1}^{N} W_\varepsilon(\mathbf{r},z)(\varepsilon_\rho)^2 + \sum_{n=1}^{N_{\Gamma_1}} \overline{W}_\varepsilon(\mathbf{r})(\overline{\varepsilon}_\rho)^2 \right\}_{(\mathrm{II})} + \left\{ \sum_{k=1}^{K} R_b(\mathbf{r},z)\|\mathbf{u}_b\|_k^2 + \sum_{n=1}^{N_{\Gamma_1}} R_u(\mathbf{r})(\nabla\mathbf{U})^2 \right\}_{(\mathrm{III})}. \tag{42}$$

The cost function contains three basic groups of terms. The first group represents weighted sums of squared differences between the "real" data (denoted by stars) and their model counterparts. The utilized data sets include:

- the Southern Ocean Hydrographic Atlas density data ρ_n^* (Olbers et al., 1992) interpolated onto the FE mesh, N is the number of the nodes of FE mesh;
- four-year mean SSH ζ_n^* derived from Topex/Poseidon altimetry available from the web site of the University of Texas, N_ζ is the number of SSH data points (Fig. 8);
- total transports U_i^* between pairs of stations on four WOCE and pre-WOCE hydrographic sections (Fig. 8) obtained by the box inverse method (Sloyan, 1997, personal communication). The section paths are shown in Fig. 8, $I_s = 136$ is the total number of the transport estimates;
- long-term annual mean wind stress data interpolated onto the surface nodes $\boldsymbol{\tau}_n^*$ (Trenberth et al., 1989), N_{Γ_1} is the number of surface nodes.

The weights W_ρ, W_u, W_τ, W_ζ define relative contribution of each observation type to the cost function. In view of the above mentioned probabilistic nature of $\mathcal{J}$ the weights W are interpreted as the inverse covariance matrices. We assume that they are diagonal i.e. observations at different locations are independent. The error variances of observations are the same for all data points of the Topex/Poseidon altimetry, wind stress data and for the transport estimates, but the error

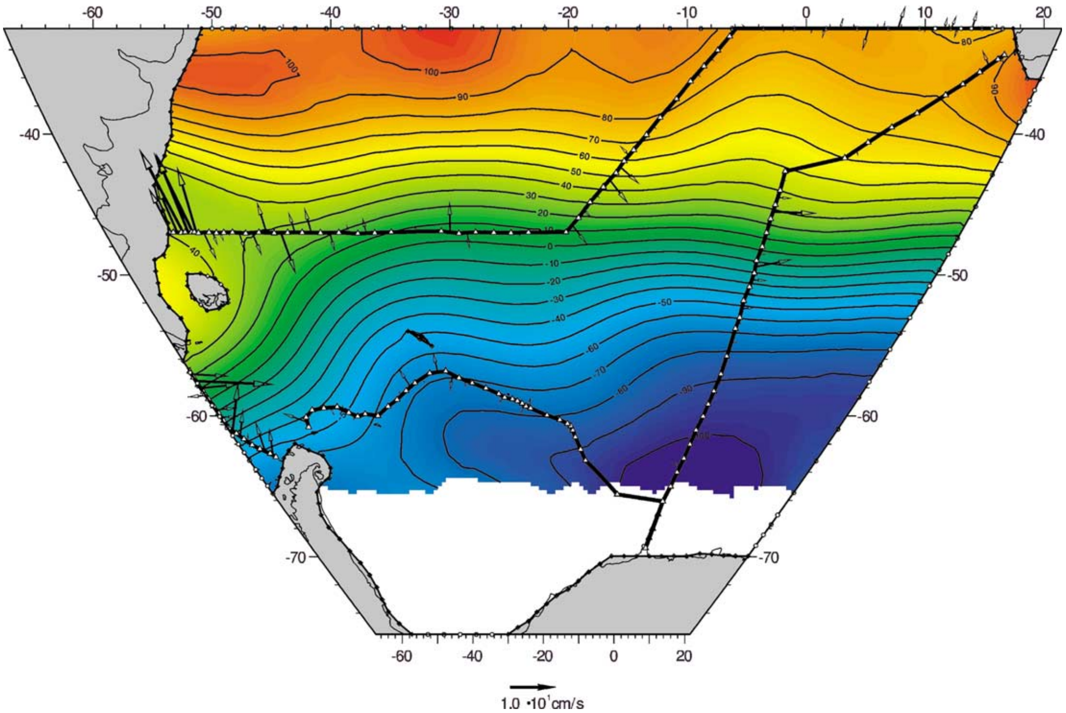

Fig. 8. Average sea surface height ζ_n^* derived from the Topex/Poseidon altimetry and paths of four hydrographic sections used in data assimilation.

variance of density data varies with depth and location. This allows us to take into account relative undersampling of polar regions and smaller variability of density data in the deep layers of the ocean.

The second group of terms in (42) penalizes residuals ε_ρ in the buoyancy conservation equation. The first term penalizes the residuals in each node with the weights W_ε depending on horizontal coordinates and depth. These weights are smaller in the weakly stratified regions, where convection events are more probable. The second term in group II introduces our expectation that the integral residuals within each water column $\overline{\varepsilon}_\rho$ should be essentially smaller than the characteristic magnitude of ε_ρ. This means that buoyancy of sea water is redistributed within a water column rather than created by the subgrid processes.

The last group represents the so-called regularization terms which penalize the amplitude of the stabilization part of the solution outside the boundary layers and the horizontal grid scale variability of the total transports $\mathbf{U} = \int_{z=-H}^{z=0} \mathbf{u}\,\mathrm{d}z$. These terms are introduced to suppress formation of artificial boundary layers near the open boundaries. As it has been discussed earlier, inconsistency between the density and wind stress distributions on one hand and normal velocities at the open boundaries on the other hand causes unrealistically strong vertical motions with fast velocity variation and, consequently, high BF component of the solution. The regularization weights R_b and R_u are significant only in the vicinity of the open boundaries.

The cost function gradient was computed using the adjoint of the tangent linear model. Constrained minimization of $\mathscr{J}$ was performed with iterative quasi-Newtonian optimization algorithm of Gilbert and Lemarechal (1989).

Optimization was performed in two stages. At the first stage the density field was held fixed and the cost function (42) was minimized with respect to open boundary velocities and wind forcing. The starting (first guess) point for the iterations was the diagnostic model solution described in the previous section. At the second stage we took into account the buoyancy conservation constraint (21) starting from the result obtained at the first step. The buoyancy diffusion coefficients in the interior of the ocean were set to $K_l = 200$ m^2/s and $K_v = 0.0001$ m^2/s. Within the top 10 m of the ocean and in the regions of low hydrostatic stability in the south K_v has been increased up to 10 times in an attempt to simulate mixing processes more realistically.

The optimized solution (Figs. 9 and 10) brings more realism to the first guess fields shown in Fig. 5. First of all, the pattern is free from strong divergences observed at the open boundaries near the coast of South America at 30°S, 40–50°W, and at the ACC outflow near 50–55°S, 21°E (Fig. 5). Currents also become more realistic in the area of the Agulhas current retroflection while the general circulation structure remains qualitatively unchanged. Mutual adjustment of the flow and density distribution reduces the amplitude of the vertical velocity in the central region of the domain (cf. Figs. 7 and 10) indicating that both branches of ACC follow isobaths more closely in the optimal solution. Also note a significant intensification of the downwelling near the Antarctic coast.

Certain important details of the circulation would have been more pronounced, if more data were available. For instance, circulation in the Weddell Sea, and especially the Weddell Gyre transport seem to be underestimated due to oversmoothing of hydrology and the absence of SSH data in that region. The authors' previous experience with the variational data analysis in the Weddell Gyre (Nechaev et al., 1995; Yaremchuk et al., 1998), which included velocities from moorings deployed at the continental shelves, supports this viewpoint.

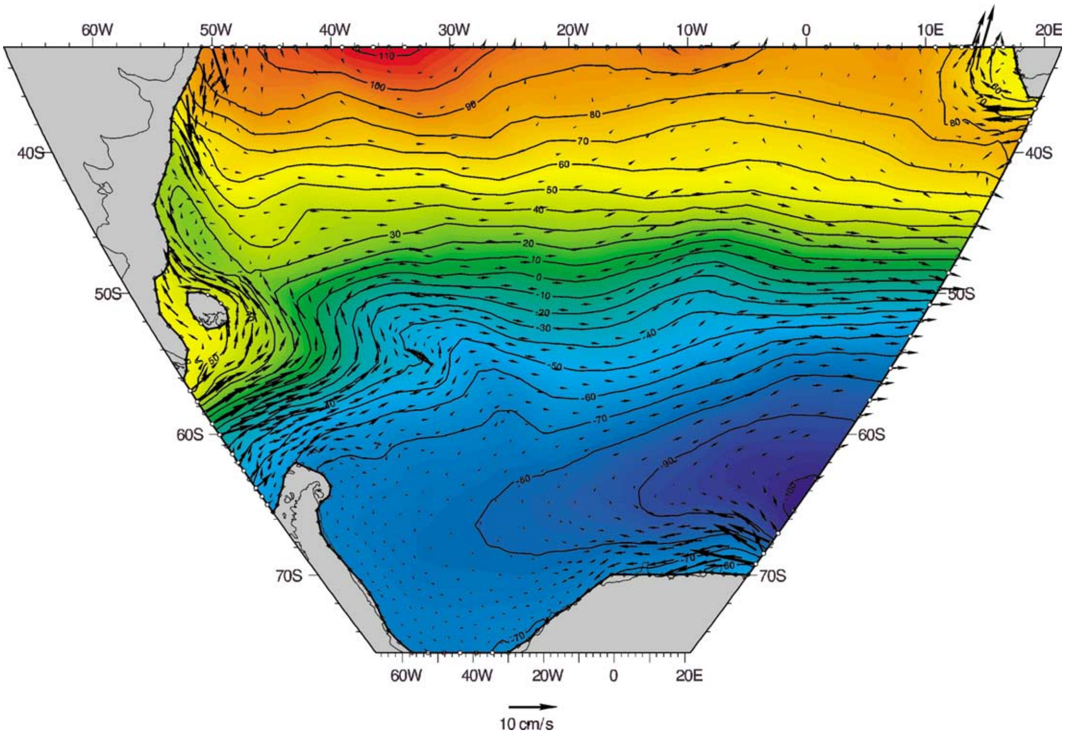

Fig. 9. Vertically averaged velocity field and sea surface height after optimization.

RMS deviation of the optimal solution from the density climatology was found to vary between 10^{-2} and 10^{-3} kg/m^3, being far within the error bars of the data. As expected, the largest model/data misfit was observed in the areas of the strong current gradients such as in the region of Agulhas current retroflection near South Africa and in the zone of separation of Brazil-Faulkland current system off the coast of South America at 39°S. We assume that the major reason for this is low spatial resolution of the climatological data. Another region of high model-data misfit is the abyssal layer of the ocean south of 55°S. This is the region where high prior density variances were prescribed due to the lack of observations. In other parts of the domain density errors are much smaller and generally reflect adjustment of the buoyancy field to the bottom topography.

The RMS deviations of the optimal state from the rest of the data were found to be 0.11 dyn/cm^2, 12 cm and 0.3 Sv for the wind stress, surface height and total transports respectively. These values also lie within the error bars indicating that the model is capable to describe the large scale ocean circulation adequately.

5. Discussion and conclusions

We have presented a stabilized FE model designed for diagnostic analysis of ocean currents at low Rossby numbers. A novel feature of the model is implementation of the bubble function

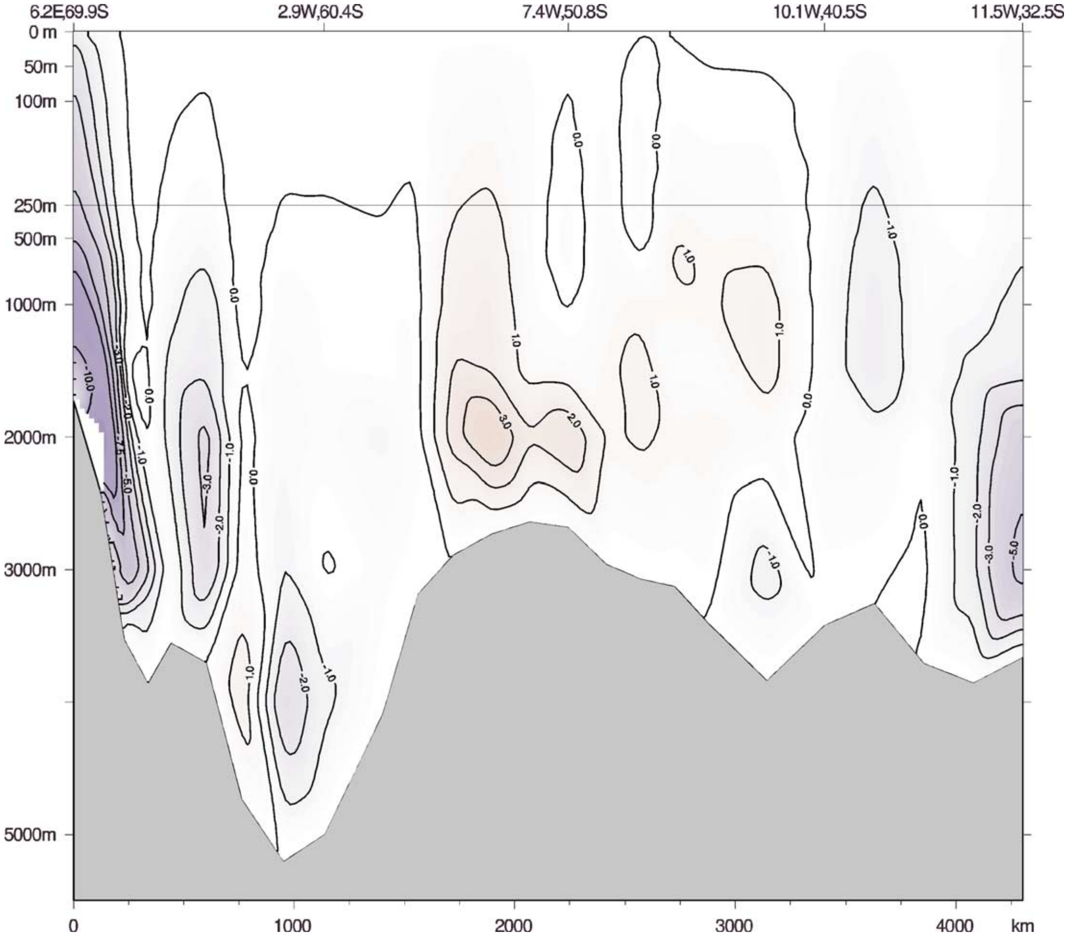

Fig. 10. Optimized vertical velocity at the section shown in Fig. 5. Contour interval is 1 × 10^{-3} cm/s.

stabilization technique. The method has been recently developed for engineering applications and provides a regular procedure for circumventing the Babuška–Brezzi compatibility condition thus giving much more freedom in the choice of FE functional spaces. Another advantage of the method is its ability to account for the influence of unresolved scales on the final solution (Russo, 1996). This influence is reflected in the BF component of the solution whose amplitude gives an objective indication of the possible inconsistencies in the model design. Another novel feature of the model is the tetrahedral unstructured FE mesh which can be viewed as an attempt for further development of the FE ocean models in the direction of enhancing their flexibility in the description of bottom topography and associated boundary layers. The model state is described in terms of piecewise linear functions which provide good computational efficiency, minimizing the number of internal degrees of freedom per element.

Numerical tests have demonstrated good model performance in approximation of the test-bed analytical solutions. The dynamically and statistically consistent test of the code against the real data has shown the model's ability to describe large scale ocean circulation within the accuracy of the error bars, typical for modern climatological data. Data assimilation has also shown that some of the unrealistic features present in the South Atlantic test solution were caused by the forcing errors.

FE models have two additional desirable characteristics which make them competitive with the traditional FD algorithms. The first one is convenience for massive parallelization. The large ratio of inter-element computation to intra-element communications suggests that such models ideally suit the parallel computing environment. This feature seems to be very important in view of the present trends in computer technology. The second advantage of the FE technique is the low cost of the adjoint code construction which is performed by direct transposition of the system matrices explicitly present in a FE model numerics. This feature is potentially useful for such important applications as model/data synthesis, dynamically constrained sensitivity analysis and posterior error estimation. To demonstrate the "adjoint-friendly" environment provided by the FE technique, we constructed a variational data assimilation scheme as one of the by-products of the code and objectively tested the model against the real data.

Although the model is formulated in a relatively general form, a number of questions are still to be addressed. The major one is the issue of bubble space parameterization. In implementing the pseudo-RFBF stabilization we have used the simplest possible approximation to the residual-free bubbles and the simplest estimate for the stabilization weights. We assume that further improvements can be made at the expense of moderate increase of the computational cost. Another important issue is the problem of 3d automated mesh generation specifically designed for oceanographic applications. In their recent work Legrand et al. (2000) proposed an algorithm for generating boundary-fitted 2d Delaunay grids on a sphere which can serve as a basis for constructing the 3d prismatic or tetrahedral grids suitable for FE discretization of the dynamics under the hydrostatic approximation. Oceanographic problems of smaller scales such as deep convection or boundary layer dynamics near steep topographic features may require 3d grids unconstrained by nodal alignment in the vertical. At present, however, there are no fully 3d FE mesh generating packages. We generated our mesh on the basis of 2d software (Joe, 1991). At the same time a large number of 3d mesh generators for engineering applications (e.g. chip design, construction, aerodynamics) are readily available. A 3d "oceanographic" grid generator can be possibly designed as a certain reduction of the existing ones. Design criteria should focus on accurate representation of the hydrostatic law in the bulk of the ocean and include an option of smooth transition to fully unstructured 3d grids in the "non-hydrostatic" regions.

The presented experience can be viewed as a first and successful attempt to utilize the RFBF method in oceanographic applications. We assume that the method has a good potential for making FEs a primary tool in global ocean modeling and data assimilation in future.

Acknowledgements

The major part of this study was completed when DN and MY were working at the Alfred-Wegener Institut für Polar und Meeresforschung (Bremerhaven, Germany). Support by the SIFAR Grant UAF-00-0080, and the Frontier System of Global Change through its funding of the

International Pacific Research Center (IPRC) was essential for completion of the research. This manuscript is an IPRC/SOEST contribution number 150/5965.

Appendix A. RFBF stabilization technique

By their definition bubble functions are functions with support confined within an element and taking zero values on its boundary ∂T_k. They were introduced to describe features of the solution "unresolvable" by the standard set of FE basis functions and by these means to improve the approximation properties of the FE method. Let V_l be the FE approximation space (e.g. the space of piecewise linears) V_b the BF space with yet undefined structure and $V_h \equiv V_l \times V_b$. Restriction of a linear problem (18) to V_h can be split into two subproblems

$$\mathscr{A}(X_l,\widetilde{X}_l) - \mathscr{R}(\widetilde{X}_l) + \sum_{k=1}^{K} \mathscr{A}(X_b^k,\widetilde{X}_l) = 0, \quad \forall \widetilde{X}_l \in \mathbf{V}_l, \tag{A.1}$$

$$\mathscr{A}(X_h^k,\widetilde{X}_b^k) - \mathscr{R}(\widetilde{X}_b^k) = 0, \quad \forall \widetilde{X}_b^k \in \mathbf{V}_b^k,\ k = 1,\dots,K. \tag{A.2}$$

Eq. (A.1) is a stabilized version of a standard Galerkin approximation $\mathscr{A}(X_l,\widetilde{X}_l) - \mathscr{R}(\widetilde{X}_l) = 0$ of (18). The terms under summation are referred to as the stabilization terms. Eq. (A.2) constrains the structure of BFs. Taking into account that $\widetilde{X}_l$ are analytical functions in T_k (A.1) can be rewritten in the standard form which has been utilized in the main body of the paper

$$\mathscr{A}(X_l,\widetilde{X}_l) - \mathscr{R}(\widetilde{X}_l) + \sum_{k=1}^{K} (X_b^k \cdot \mathscr{L}^{\dagger}\widetilde{X}_l) = 0, \quad \forall \widetilde{X}_l \in \mathbf{V}_l. \tag{A.3}$$

The idea of RFBF method is to define the shape of BFs by elementwise solution of (A.2) in the strong form: $X_b = \mathscr{L}^{-1}[\mathscr{R} - \mathscr{L}X_l]$. In other words, the RFBFs are designed to eliminate the residuals $\mathbf{r} \equiv \mathscr{L}X_l - \mathscr{R}$ of the Galerkin approximation to the original system. Since X_l is represented in T_k by a finite number n of the basis functions $\boldsymbol{\varphi}^i$, $i = 1,\dots,n$, $\dim\mathbf{V}_b \leqslant n$ and a set of basis functions $\boldsymbol{\varphi}_b^i$ in $\mathbf{V}_b$ can be found by solving the following boundary value problems:

$$\mathscr{L}\boldsymbol{\varphi}_b^i = -\boldsymbol{\varphi}^i; \quad \boldsymbol{\varphi}_b^i(\partial T_k) = 0. \tag{A.4}$$

The pseudo-RFBF method (Brezzi et al., 1996b) is based upon the solution of (A.2) in the weak form, often with reduced dimension of V_b, i.e. only a limited set of the bubble basis functions is taken into the account which corresponds to $\boldsymbol{\varphi}^i$'s with the slowest variability within an element.

To derive (26), we consider just two bubble basis functions, which provide the solution of (A.2) in the form

$$\mathbf{v}_b^k = -\varepsilon_1[(\mathbf{r}\cdot\boldsymbol{\varphi}_b^1)_k\boldsymbol{\varphi}_b^1 + (\mathbf{r}\cdot\boldsymbol{\varphi}_b^2)_k\boldsymbol{\varphi}_b^2] - \varepsilon_2[(\mathbf{r}\cdot\boldsymbol{\varphi}_b^2)_k\boldsymbol{\varphi}_b^1 - (\mathbf{r}\cdot\boldsymbol{\varphi}_b^1)_k\boldsymbol{\varphi}_b^2], \tag{A.5}$$

where $\varepsilon_{1,2}$ are given by (35) and

$$s_k = \left[A_l|\nabla\boldsymbol{\varphi}_b|^2 + A_v|\partial_z\boldsymbol{\varphi}_b|^2\right]|f|^{-1}|\boldsymbol{\varphi}_b|^{-2}.$$

Substituting (A.5) into (A.3) and taking into the account orthonormality of the bubble basis functions yields (26).

Appendix B. Computation of the advective velocities and conservation laws

To project the solution $\mathbf{u}_h$ of momentum equations (18) onto the set of elementwise constant velocities $\mathbf{U}_c(\mathscr{T}_\Omega)$ we solve the following weak problem: find $\mathbf{u}_c \in \mathbf{U}_c$, such that

$$\int_\Omega \{\mathbf{u}_c\tilde{\mathbf{u}}_c - (\mathbf{v}_l + \mathbf{v}_b + \mathbf{v}_\gamma)\tilde{\mathbf{u}}_c\}\,\mathrm{d}\Omega = 0, \quad \forall\tilde{\mathbf{u}}_c \in \mathbf{U}_c. \tag{A.6}$$

Similarly to (26) the inner product $(\mathbf{v}_b \cdot \tilde{\mathbf{u}}_c) = \int_\Omega \mathbf{v}_b\tilde{\mathbf{u}}_c\,\mathrm{d}\Omega$ in (A.6) can be estimated as

$$(\mathbf{v}_b \cdot \tilde{\mathbf{u}}_c) = \sum_{k=1}^{K}[-\epsilon_1^k(\mathbf{r}^k \cdot \tilde{\mathbf{u}}_c)_k + \epsilon_2^k(\mathbf{k} \times \mathbf{r}^k \cdot \tilde{\mathbf{u}}_c)_k]. \tag{A.7}$$

The resulting elementwise constant velocity $\mathbf{u}_c$ satisfies the integral volume conservation constraint in the form

$$-\int_\Omega \mathbf{u}_c\nabla\tilde{\zeta}_l\,\mathrm{d}\Omega + \int_{\Gamma_3} \mathbf{v}_\gamma\tilde{\zeta}_l\mathbf{n}\,\mathrm{d}\gamma_3 = \int_{\Gamma_1} F_\zeta\tilde{\zeta}_l\,\mathrm{d}\gamma_1, \quad \forall\tilde{\zeta}_l \in P_l. \tag{A.8}$$

The relationship (A.8) follows from the stabilized momentum problem (24)–(26) written for the test vector $\widetilde{X}_l = \{\mathbf{0}, \tilde{\zeta}_l\}$:

$$\int_\Omega g(\mathbf{v}_l + \mathbf{v}_b)\nabla\tilde{\zeta}_l\,\mathrm{d}\Omega + \int_\Omega g\mathbf{v}_\gamma\nabla\tilde{\zeta}_l\,\mathrm{d}\Omega - \int_{\Gamma_3} g\mathbf{v}_\gamma\tilde{\zeta}_l\mathbf{n}\,\mathrm{d}\gamma_3 + \int_{\Gamma_1} gF_\zeta\tilde{\zeta}_l\,\mathrm{d}\gamma_1 = 0, \quad \forall\tilde{\zeta}_l \in P_l. \tag{A.9}$$

By definition of the projection (A.6) we have

$$\int_\Omega \mathbf{u}_c\nabla\tilde{\zeta}_l\,\mathrm{d}\Omega = \int_\Omega (\mathbf{v}_l + \mathbf{v}_b + \mathbf{v}_\gamma)\nabla\tilde{\zeta}_l\,\mathrm{d}\Omega, \quad \forall\tilde{\zeta}_l \in P_l.$$

Combining the latter expression with (A.9) we arrive at (A.8).

To compute vertical velocity we integrate the continuity equation (7) with the boundary condition (10). To avoid singularity in the approximation of the first order problem (7) and (10), we introduce an auxiliary variable Φ, such that $w = \partial_z\Phi$. This converts (7), (10) and (11) into the second-order problem with two Neumann boundary conditions

$$\partial_{zz}^2\Phi - \nabla \cdot \mathbf{u} = 0; \quad \partial_z\Phi(\Gamma_1) = F_\zeta; \quad \partial_z\Phi(\Gamma_2) = 0,$$

and solvability condition (2). The FE approximation of this step is formulated as follows: find $\Phi_l \in \mathbf{U}_l(\mathscr{T}_\Omega)$, such that

$$\int_\Omega \{-\partial_z\Phi_l\partial_z\tilde{\Phi}_l - \mathbf{u}_c\nabla\tilde{\Phi}_l\}\,\mathrm{d}\Omega + \int_{\Gamma_3} \mathbf{v}_\gamma\tilde{\Phi}_l\mathbf{n}\,\mathrm{d}\gamma_3 - \int_{\Gamma_1} F_\zeta\tilde{\Phi}_l\,\mathrm{d}\gamma_1 = 0, \quad \forall\tilde{\Phi}_l \in \mathrm{U}_l. \tag{A.10}$$

The solvability condition for (A.10) coincides with (A.8) and holds for all $\mathbf{u}_c$ obtained as the projection (A.6) of $\mathbf{u}_h$. Vertical velocity can now be obtained as a function $w_c \in \mathrm{U}_c(\mathscr{T}_\Omega)$ satisfying

$$\int_\Omega (w_c\tilde{w}_c - \partial_z\Phi_l\tilde{w}_c)\,\mathrm{d}\Omega = 0, \quad \forall\tilde{w}_c \in \mathbf{U}_c. \tag{A.11}$$

To conserve the net mass of a tracer in the absence of boundary fluxes advective velocities must satisfy the constraint

$$\int_{\Omega} (\mathbf{u}_c \nabla C_l^m + w_c \partial_z C_l^m) \, \mathrm{d}\Omega = 0 \quad \forall C_l^m \in \mathbf{U}_l, \tag{A.12}$$

which follows from (27) written down for the test function $\widetilde{C}_l^m = 1$ everywhere in Ω and zero surface fluxes q_l^m (for simplicity we assume that our domain has no open boundary). Stabilization terms in (27) do not contribute to (A.12) since $\mathscr{L}_{\mathcal{C}}^{\dagger} \widetilde{C}_l^m \equiv 0$ for any $(\widetilde{C}_l^m)_k = \text{const}$ in T_k.

Let us check if (A.12) is valid for $(\mathbf{u}_c, w_c)$. Since $\tilde{\Phi}_l$ in (A.10) and C_l^m in (A.12) both belong to the same space U_l, the first term under the integral in (A.12) can be written as $-\partial_z \Phi_l \partial_z \tilde{\Phi}_l$, while the second term is equal to $w_c \partial_z \tilde{\Phi}_l$. Then the condition (A.12) takes the form

$$\int_{\Omega} (-\partial_z \Phi_l + w_c) \partial_z \tilde{\Phi}_l \, \mathrm{d}\Omega = 0, \quad \forall \tilde{\Phi}_l \in \mathbf{U}_l. \tag{A.13}$$

Since $\partial_z \tilde{\Phi}_l$ is constant on each element T_k, we conclude that $\partial_z \tilde{\Phi}_l \in \mathbf{U}_c$ i.e. (A.13) is equivalent to (A.11). Consequently (A.12) is valid $\forall C_l^m \in \mathbf{U}_l$ and our advective velocity is non-divergent in the sense of the divergence operator introduced by the tracer conservation equation.

References

Babuška, I., 1971. Error bounds for finite-element method. Numer. Math. 16, 322–333.

Brezzi, F., Franca, L.P., Hughes, T.J.R., Russo, A., 1996a. Stabilization technique and subgrid scales capturing. In: The State of the Art in Numerical Analysis, based on the proceedings of the Conference on the State of the Art in Numerical Analysis, York, England, April 1996. In: Duff, I.S., Watson, G.A. (Eds.), IMA Conference Series, 63. Oxford University Press, pp. 391–406.

Brezzi, F., Marini, D., Russo, A., 1996b. Pseudo residual-free bubbles and stabilized methods. In: Désideri, J.A. et al. (Eds.), Computational Methods in Applied Sciences. John Wiley & Sons, pp. 3–8.

Brezzi, F., Franca, L.P., Hughes, T.J.R., Russo, A., 1997. $b = \int g$. Comput. Meth. Appl. Mech. Eng. 145, 329–339.

Franca, L.P., Russo, A., 1996a. Approximation of the Stokes problem by residual-free macro bubbles. East–West J. Numer. Anal. 4, 265–278.

Franca, L.P., Russo, A., 1996b. Deriving upwinding, mass lumping and selective reduced integration by residual free bubbles. Appl. Math. Lett. 9, 83–88.

Franca, L.P., Russo, A., 1997. Unlocking with residual-free bubbles. Comput. Meth. Appl. Mech. Eng. 142, 361–364.

Gilbert, J.Ch., Lemarechal, C., 1989. Some numerical experiments with variable-storage quasi-Newton algorithms. Math. Program. 45, 407–435.

Greenberg, D.A., Werner, F.E., Lynch, D.R., 1998. A diagnostic finite-element ocean circulation model in spherical-polar coordinates. J. Atmos. Oceanic Technol. 15, 942–958.

Griffies, S.M., Böning, C., Bryan, F.O., Chassignet, E.P., Gerdes, R., Hasumi, H., Hirst, A., Treguier, A.-M., Webb, D., 2000. Developments in ocean climate modelling. Ocean Modell. 2, 123–192.

Ishizaki, H., 1994. A simulation of the abyssal circulation in the North Pacific ocean. J. Phys. Oceanogr. 24, 1941–1954.

Iskandarani, M., Haidvogel, D.B., Boyd, J., 1995. A staggered spectral element model for the shallow water equations. Int. J. Numer. Meth. Fluids 20, 393–414.

Joe, B., 1991. `GEOMPACK`—a software package for the generation of meshes using geometric algorithms. Adv. Eng. Software 13, 325–331.

Legrand, S., Legat, V., Deleersnijder, E., 2000. Delaunay mesh generation for an unstructured-grid ocean general circulation model. Ocean Modell. 2, 17–28.

Le Provost, C., Poncet, A., 1978. Finite element method for spectral modelling of tides. Int. J. Numer. Meth. Eng. 12, 853–871.

Le Roux, D.Y., Stanforth, A., Lin, C.A., 1998. Finite elements for Shallow water equation ocean models. Mon. Weather Rev. 126, 1931–1951.

Le Roux, D.Y., Lin, C.A., Stanforth, A.., 2000. A semi-implicit semi-lagrangian shallow-water ocean model. Mon. Weather Rev. 128, 1384–1401.

Lyard, F., 1997. The tides in the Arctic ocean from a finite element model. J. Geophys. Res. 102 (C7), 15611–15638.

Lyard, F., Genco, M.L., 1994. Optimization methods for bathymetry and ocean boundary conditions in a finite element model of ocean tides. J. Comput. Phys. 114, 234–256.

Lynch, D.R., Gray, W.G., 1979. A wave-equation model for finite-element tidal computations. Comput. Fluids 7, 207–228.

Lynch, D.R., Ip, J., Namie, C., Werner, F., 1996. Comprehensive coastal circulation model with application to the Gulf of Main. Continent. Shelf Res. 16, 875–906.

Myers, P.G., Weaver, A.J., 1995. A diagnostic barotropic finite-element ocean circulation model. J. Atmos. Oceanic Technol. 12, 511.

Nechaev, D.A., Yaremchuk, M., Schröter, J., 1995. A steady state inverse model of the large scale circulation in the Weddell Sea. WOCE Newsletter, WOCE Int. Project Office, Southampton, UK, vol. 21, pp. 11–14.

NOAA, ETOP05 digital relief of the surface of the earth data announcement, 1986. NOAA Tech. Report 86-MGG-07, Nat. Geophys. Data Center, Washington, DC.

Olbers, D., Gouretski, V., Seiss, G., Schroeter, J., 1992. Hydrographic Atlas of the Southern Ocean. Alfred-Wegener-Institut für Polar- und Meeresforschung, Bremerhaven.

Pierre, R., 1995. Optimal selection of the bubble function in the stabilization of the P1–P1 element for the Stokes problem. SIAM J. Numer. Anal. 32, 1210–1224.

Reid, J.L., 1989. On the total geostrophic circulation in the South Atlantic Ocean: Flow patterns, tracers and transports. Prog. Oceanogr. 23 (3), 149–244.

Russo, A., 1996. A posteriori error indicators via bubble functions. Math. Models Meth. Appl. Sci. 6, 33–41.

Saad, Y., 1993. A flexible inner–outer preconditioned GMRES algorithm. SIAM J. Sci. Statist. Comput. 14, 461–469.

Sentchev, A., Yaremchuk, M.I., 1999. Tidal motions in the Dover Straits as a variational inverse of the sea level and surface velocity data. Continent. Shelf Res. 19, 1905–1932.

Sloyan, B., 1997. Personal communication.

Stutser, S., Krauss, W., 1998. Mean circulation and transports in the South Atlantic Ocean: Combining model and drifter data. J. Geophys. Res. 103 (C13), 30985–31002.

Thacker, W.C., 1989. On the role of Hessian matrix in fitting models to data. J. Geophys. Res. 94, 6177–6196.

Trenberth, K., Olson, J., Large, W., 1989. A Global Ocean Wind Stress Climatology based on ECMWF Analyses. Tech. Rep. NCAR/TN-338+STR, National Center for Atmospheric Research Boulder, Colorado.

Yaremchuk, M.I., Nechaev, D.A, Schröter, J., Fahrbach, E., 1998. A dynamically consistent analysis of circulation and transports in the southwestern Weddell Sea. Ann. Geophys. 16, 1024–1038.